

# Thermodynamics of Antisite Defects in Layered NMC Cathodes: Systematic Insights from High-Precision Powder Diffraction Analyses

Liang Yin, Zhuo Li, Gerard S. Mattei, Jianming Zheng, Wengao Zhao, Fredrick Omenya, Chengcheng Fang, Wangda Li, Jianyu Li, Qiang Xie, Evan M. Erickson, Ji-Guang Zhang, M. Stanley Whittingham, Ying Shirley Meng, Arumugam Manthiram, and Peter G. Khalifah\*

Cite This: <https://dx.doi.org/10.1021/acs.chemmater.9b03646>

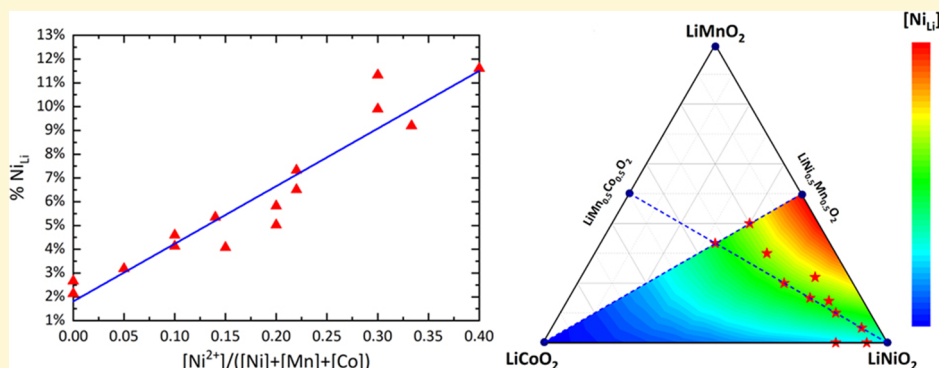
Read Online

ACCESS |

Metrics & More

Article Recommendations

Supporting Information



**ABSTRACT:** While it is accepted that paired Ni<sub>Li</sub> and Li<sub>Ni</sub> antisite defects are present in the important family of NMC cathode materials with the general formula Li(Ni<sub>x</sub>Mn<sub>y</sub>Co<sub>z</sub>)O<sub>2</sub>, their formation mechanism and influence on properties are not well understood due to the difficulty of accurately quantifying defects. In this work, novel high-precision powder diffraction methods have been used to elucidate the dependence of defect concentration on NMC composition. Formation energies for paired antisite defects (calculated under the assumption of equal state degeneracy) are observed to vary from about 320 to 160 meV, contradicting the constant defect formation energy that would be expected based on the previously proposed atomistic defect formation mechanism (size similarity of Ni<sup>2+</sup> and Li<sup>+</sup> cations). The present data support an alternative mechanism in which the equilibrium defect concentration is determined by the average size of transition-metal sites and thus suggest a new route by which chemical substitutions can be used to tune defect concentrations to optimal levels.

## INTRODUCTION

Many emerging transformative technologies (mobile electronics, electric vehicles, unmanned aerial vehicles, etc.) require energy storage with both high energy density and high power density. For many applications, these two needs are best met through the use of Li-ion batteries. Intensive research efforts are ongoing to further improve the performance of Li-ion batteries to enable longer device lifetimes, extended vehicle ranges, and longer time airborne. To meet these goals, it is particularly critical to improve the performance of cathode materials as they typically have an energy density lower than that of their partner anode materials by a factor of 2 or more.

The NMC family of layered materials with a general formula of Li(Ni<sub>x</sub>Mn<sub>y</sub>Co<sub>z</sub>)O<sub>2</sub> represents one of the most promising families of cathode materials for applications in the near term as these materials provide high specific capacities (>200 mA h/g) with average voltages near 4 V that can be accessed using relatively short charge and discharge times (of 1 h or less).

Early industrial interest in this family of compounds focused on the material LiCoO<sub>2</sub>, which has both good ionic conductivity and good electronic conductivity. However, the high cost and limited availability of Co spurred the later development of alternative layered materials with lower Co contents through the substitution of Co<sup>3+</sup> by Ni<sup>3+</sup> and/or Mn<sup>4+</sup> (which is charge-balanced through the reduction of an equivalent number of Ni<sup>3+</sup> ions to Ni<sup>2+</sup>). In recent years, many of these efforts focused on Ni-rich chemistries, which provide some of the highest achievable energy densities, though with the tradeoff of having more challenges associated with their synthesis, processing, lifetime, and safety. It is expected that some of

Received: September 5, 2019

Revised: December 21, 2019

Published: December 23, 2019

these challenges can be mitigated through appropriate design strategies such as optimizing the NMC composition, introducing appropriate dopants, or controlling the concentration of key defects. While the first two approaches have been extensively pursued, the last approach of controlling defect concentrations remains relatively unexplored due to the challenges of quantifying defect concentrations accurately.

Pristine NMC compounds typically adopt the  $\alpha$ -NaFeO<sub>2</sub> structure type, which is an ordered variant of the rock-salt structure type in which the Li<sup>+</sup> cations and transition-metal (TM) cations are segregated into separate layers instead of being randomly mixed as they would be in the simpler rock-salt structure type exemplified by  $\alpha$ -LiFeO<sub>2</sub> (Figure S1). In addition to having full cation ordering and no cation ordering, it is common for partial cation ordering within the  $\alpha$ -NaFeO<sub>2</sub> structure to occur through the formation of paired antisite (PAS) defects, which are expected to preferentially occur as Li<sub>Ni</sub> and Ni<sub>Li</sub> pairs due to the Ni cations (especially when present as Ni<sup>2+</sup>) being closer in size to Li<sup>+</sup> than to the Co<sup>3+</sup> or Mn<sup>4+</sup> cations. While PAS defects do not affect the stoichiometry, a variety of other non-stoichiometric defects may occur within the  $\alpha$ -NaFeO<sub>2</sub> structure type. In general, Li vacancy compositions of [Li<sub>1-x</sub>][TM]O<sub>2</sub> are intentionally accessed during electrochemical cycling but may also inadvertently be produced prior to cycling if synthesis and storage conditions are not well controlled. Additionally, it is specifically known that compositions near LiNiO<sub>2</sub> often have excess Ni with compositions such as [Li<sub>1-x</sub>Ni<sub>x</sub>][Ni]O<sub>2</sub>.<sup>1</sup> Related Li-excess compounds, [Li][Li<sub>x</sub>TM<sub>1-x</sub>]O<sub>2</sub>, have been intentionally prepared and extensively investigated for battery applications due to their high specific capacities.<sup>1-3</sup> While oxygen vacancies (LiTMO<sub>2-x</sub>) have been proposed based on chemical analyses, we are unaware of robust structural evidence for the existence of these defects in pristine NMC compounds, and it is notable that oxygen vacancy defects were not observed during powder neutron diffraction studies of such phases despite the high sensitivity of neutrons to scattering from oxygen atoms.

## EXPERIMENTAL SECTION

Altogether, 17 NMC samples with 11 different nominal compositions were obtained from a variety of sources. Some were obtained from industrial suppliers. Others were synthesized within academic research laboratories. The details of these sample nominal compositions and their synthesis conditions are given in Table S1. Samples had only trace amounts of impurities, which were neglected in Rietveld analyses due to their small amount and minimal overlap with NMC phases.

High-resolution synchrotron X-ray powder diffraction data were collected at the 11-BM beamline at the Advanced Photon Source (APS) of Argonne National Laboratory ( $\lambda = 0.412721, 0.414576, 0.412688, 0.457658, \text{ or } 0.412813 \text{ \AA}$ ). Samples were loaded in 0.8 mm Kapton capillaries (Cole-Parmer; 1/32 in. ID and 1/30 in. OD). Experimental tests showed that the capillary loading typically resulted in a 48% ( $\pm 2\%$ ) packing density, a value which was used to calculate the absorption cross section and to apply a cylindrical absorption correction for all synchrotron samples. Structures were refined using the Rietveld method as implemented in the TOPAS software package (Bruker-AXS, version 6) across a  $d$ -spacing range of 5.0 to 0.5  $\text{\AA}$ .

Time-of-flight (TOF) neutron powder diffraction experiments were performed on the NOMAD diffractometer at the Spallation Neutron Source (SNS), Oak Ridge National Laboratory (ORNL) during the 2017-A, 2017-B, and 2018-B run cycles. About 100 mg of powder were packed in a 3 mm diameter thin-walled fused quartz capillary from Charles Supper Company. Typical data acquisition times of 100 min were used. NOMAD data were normalized against a vanadium

rod and reduced using custom beamline IDL software.<sup>4</sup> The neutron coherent scattering lengths (Li: -1.90 fm, Ni: 10.3 fm, Mn: -3.73 fm, Co: 2.49 fm, O: 5.803 fm) vary irregularly with atomic number and isotope and are essentially independent of  $d$  spacing. TOF neutron diffraction data were fit using the Rietveld method as implemented in the TOPAS software package (Bruker-AXS, version 6) over a  $d$ -spacing range of 2.6 to 0.2  $\text{\AA}$ , using data from the three highest angle banks with central  $2\theta$  angles of 65 (bank 3), 120.4 (bank 4), and 150.1° (bank 5). The diffraction peak shapes were primarily modeled using a pseudo-Voigt function with convolutions to model the moderator-induced asymmetrical peak shape, with a representative TOPAS input file provided in the Supporting Information.

## RESULTS AND DISCUSSION

**Quantification of NMC Occupancy Defects.** The accurate classification and quantification of site occupancy defects in NMC cathode materials is a challenging exercise when powder samples are studied due to the generic limitations of powder diffraction techniques.<sup>5-8</sup> Most prior studies of NMC defects were done using conventional Cu  $K\alpha$  laboratory powder diffraction data,<sup>9-25</sup> which are limited both in range ( $d_{\text{min}} \sim 0.9 \text{ \AA}$ ) and in signal/noise ratio and are therefore not suitable for sensitively probing defects. There have been a relatively small number of structural studies that utilized the more informative synchrotron<sup>26-28</sup> or neutron<sup>11,16,26,27,29</sup> diffraction data to study NMC materials, though these studies have universally been narrow in scope. It is not possible to obtain an accurate systematic understanding of defects by comparing these isolated studies because the errors associated with different instrumental and sample configurations are often large relative to the statistical errors inherent to the data itself.

In order to, for the first time, gain a comprehensive understanding of occupancy defects in NMC compounds, we carried out a comparative structural study of 17 NMC samples spanning a wide range of compositions with the Ni fraction relative to the total TM content ranging from  $\chi_{\text{Ni}} = 0.33$  (LiNi<sub>0.33</sub>Mn<sub>0.33</sub>Co<sub>0.33</sub>O<sub>2</sub>) to  $\chi_{\text{Ni}} = 0.94$  (LiNi<sub>0.94</sub>Co<sub>0.06</sub>O<sub>2</sub>) using two complementary types of data from advanced user facilities. Compounds were investigated using both high-resolution synchrotron X-ray (11-BM) and time-of-flight neutron (NOMAD) powder diffraction data analyzed through Rietveld refinements, with representative fits shown in Figure S2. While the individual advantages of synchrotron data ( $d_{\text{min}} \sim 0.5 \text{ \AA}$ , negligible instrumental peak broadening, excellent counting statistics, limited absorption, and very similar scattering powers for the three transition metals) and neutron data ( $d_{\text{min}} \sim 0.2 \text{ \AA}$ , high sensitivity to O and Ni, low absorption, negligible preferred orientation, and very different scattering powers for the three transition metals) are substantial, the simultaneous study of these two different types of data enables additional sensitivity in distinguishing between different possible defect models and gives additional confidence in results that are common across the independent sources of data. Structural refinements were carried out using the conventional  $R\text{-}3m$  space group ( $a \sim 2.8 \text{ \AA}$ ;  $c \sim 14 \text{ \AA}$ ) for the  $\alpha$ -NaFeO<sub>2</sub> family of compounds for which there are three types of crystallographic sites: those of Li (3a), the TMs (3b), and O (6c).

Any defect that modifies the occupancy of one or more crystallographic sites within this structure type will be generically termed an occupancy defect. While it is normally difficult to accurately identify and quantify occupancy defects, we have recently developed a new methodology ( $f^*$  diagrams) for doing so that allows the determination of antisite defect

concentrations in NMC compounds with exceptional precision (agreement of 0.1% absolute between synchrotron and neutron refinements) after correcting for errors in the standard X-ray form factor for oxygen.<sup>30</sup> These  $f^*$  diagrams graphically represent the two total degrees of freedom associated with the occupancies of the three crystallographic sites in the NMC structure type on a triangular plot analogous to those used for phase diagrams. The coordinates along the edge associated with each of the three crystallographic sites represent the fractional contribution of each crystallographic site relative to the total scattering power of the structure ( $F_{000}$ ) at a  $2\theta$  angle of  $0^\circ$ . In this manner, it is possible to graphically visualize the effect of different occupancy defects as vectors in this coordinate space (Figure S3) and to unambiguously identify the nature and amount of defects present in NMC samples.

For the 17 NMC samples, it was found that occupancy defects are present in all samples and that paired antisite (PAS) defects of  $\text{Ni}_{\text{Li}}$  and  $\text{Li}_{\text{Ni}}$  are the overwhelmingly dominant defects affecting the refinement in all cases except for two commercial samples of NMC333. The importance of Ni/Li PAS defects can be seen in  $f^*$  diagrams constructed using both synchrotron (Figure 1a) and neutron (Figure 1b) diffraction data for a representative compound of NMC622, which show that the global minimum fit in this two-dimensional parameter space (blue circle, achievable by varying site occupancies in any double-defect refinement in which the amounts of two different classes of occupancy defects are freely refined) is very closely reproduced when using Ni/Li PAS as the only occupancy defect type. Furthermore, it can be unambiguously resolved that the Li paired antisite defects predominantly involve Ni rather than Mn or Co as Ni is the only transition metal that gives agreement in the PAS defect concentration refined independently from X-ray and neutron data (Table S2) for this NMC622 sample.

The dominant influence of Ni/Li PAS defects across the entire series of NMC samples is seen in Figure 2a, which shows the percentage of the global maximum improvement in synchrotron X-ray refinement  $R_{\text{wp}}$ , where 0% corresponds to the  $R_{\text{wp}}$  of the ideal structural model and 100% corresponds to the global minimum  $R_{\text{wp}}$  obtained using double-defect models (values given in Table S3 and alternate plots using conventional X-ray atomic form factors in Figure S4). For most compounds, the use of these antisite defects alone gave 98–100% of the possible improvement in  $R_{\text{wp}}$  relative to the global maximum. However, the two commercial samples of nominal composition  $\text{Li}(\text{Ni}_{1/3}\text{Mn}_{1/3}\text{Co}_{1/3})\text{O}_2$  studied in this work were clear outliers to this trend. Similar results were found for refinements against neutron data (Figure 2b), though the improvement in single-defect (Ni/Li PAS) refinement  $R_{\text{wp}}$  was a lower fraction of the global maximum (90–100%), presumably due to the high sensitivity of neutron refinements to small amounts of transition-metal off-stoichiometry, something that X-ray refinements are very insensitive to. A preliminary analysis suggests that these two NMC333 compounds contain a substantial Li excess (5–8%) and thus fall outside of the baseline NMC stoichiometries of  $\text{Li}(\text{Ni}_x\text{Mn}_y\text{Co}_z)\text{O}_2$ . For this reason, these two NMC333 samples were omitted from the analysis of trends in the next section, though a third NMC333 stoichiometric sample was still available for this analysis.

The refined quantity of Ni/Li paired antisite defects for the 15 stoichiometric NMC samples is plotted in Figure 3, which shows a comparison of the defect fractions independently

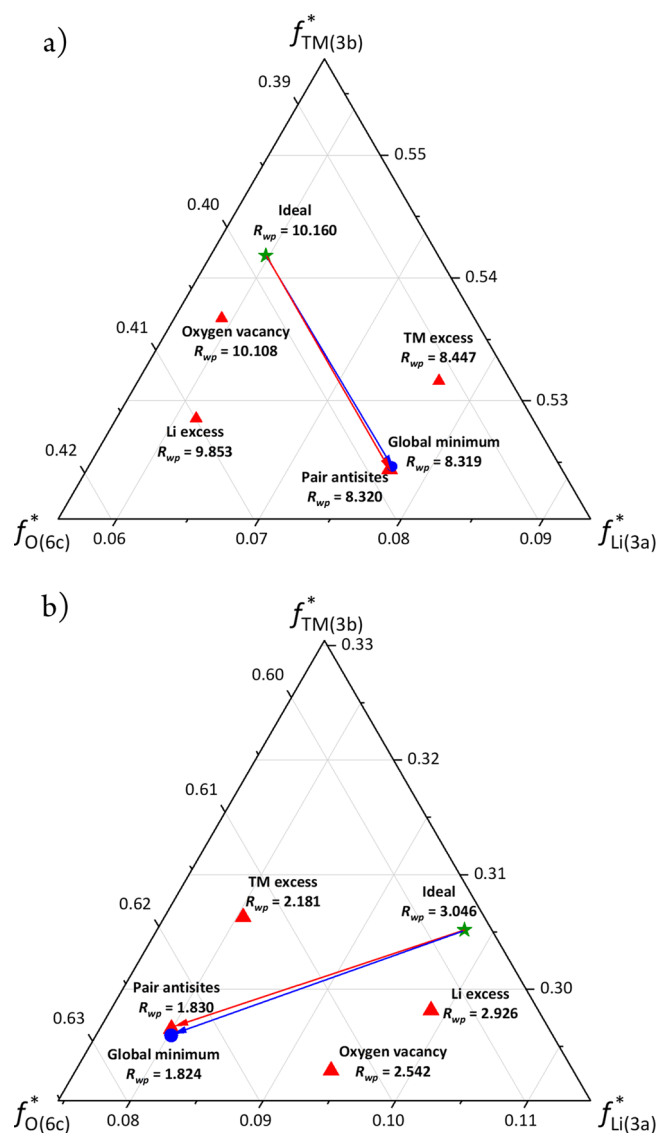


**Figure 1.**  $f^*$  diagrams for  $\text{Li}(\text{Ni}_{0.6}\text{Mn}_{0.2}\text{Co}_{0.2})\text{O}_2$  calculated for (a) X-ray and (b) neutron data. The  $f^*$  coordinates based on the ideal composition are marked with a green star, those experimentally obtained from four different single-defect refinements are marked with red triangles, and the global minimum (obtained through a double-defect refinement) is marked with a blue circle. The single-defect model of paired antisite defects alone effectively reproduces the global best result in both  $f^*$  coordinates and  $R_{\text{wp}}$  value and is thus the dominant defect.

refined from X-ray (blue) and neutron (red) powder diffraction data. Superb sensitivity to defects was obtained using refinements that we optimized in ways that differ from the prior literature, including (1) using optimal atomic form factors, (2) using parametrically refined atomic displacement parameters (ADPs) extracted from neutron diffraction data, and (3) using high-quality user facility data for which aberrations for sample absorption have been either rigorously corrected (X-ray) or effectively minimized (neutron), as described in detail elsewhere.<sup>30</sup> In the absence of these optimizations, the systematic errors in extracted defect concentrations can easily be higher by an order of magnitude or more. Using our methods, the average difference between the Ni/Li PAS fraction refined independently from neutron and X-ray data for these 15 NMC samples is only 0.16%

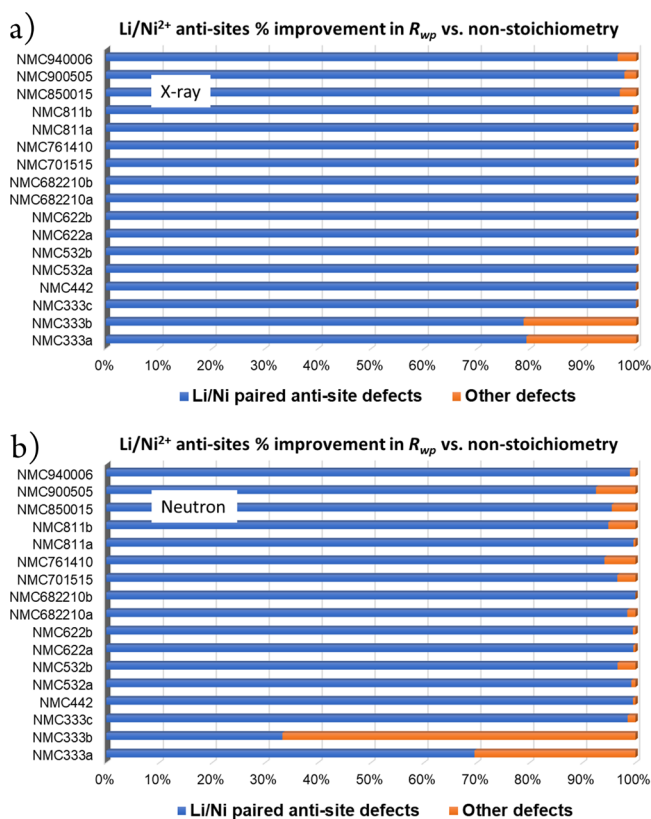


**Figure 2.** Bar plots of the relative improvement in refinement  $R_{wp}$  for 17 NMC samples from adding a single-defect model of paired antisite  $\text{Li}_{\text{Ni}}$  and  $\text{Ni}_{\text{Li}}$  defects to the structural model using (a) X-ray data or (b) neutron data. Improvements are relative to the  $R_{wp}$  obtained without including defects (0%) and are normalized to the  $R_{wp}$  improvement obtained using the global minimum fit (from a double-defect refinement), which was taken to represent a 100% improvement. X-ray refinements were carried out using neutral atomic form factors for all elements except oxygen, for which the ionic ( $\text{O}^{2-}$ ) form factor was used. A bar plot generated using conventional neutron X-ray atomic form factors is provided in Figure S4 for comparison. Data used for the plots is given in Table S4.

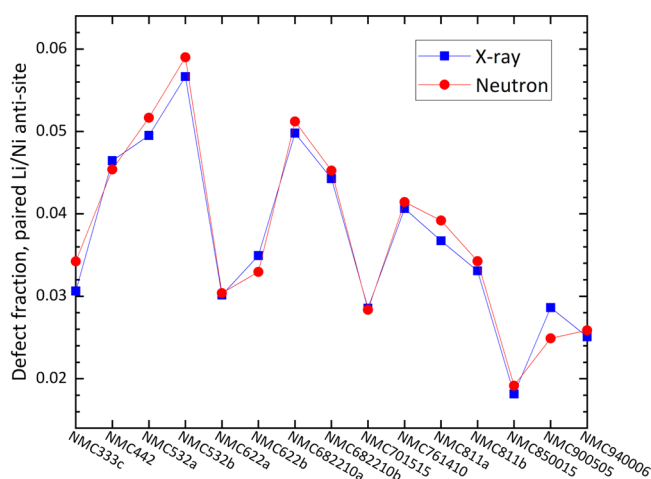


**Figure 3.** Comparison of the Ni/Li paired antisite defect concentrations refined from X-ray (blue) and neutron data (red) for the 15 stoichiometric NMC samples examined in this work. The average difference in defect fraction is 0.16% (absolute).

(absolute), demonstrating an exceptional level of sensitivity in quantifying these defects, which enables unprecedented insights into structure–property correlations.

**Origin and Prediction of PAS Defects.** While it is generally accepted that  $\text{Ni}^{2+}$  plays an important role in governing the paired antisite defect concentration in NMC compounds, to date, there is no comprehensive understanding of the mechanism by which this occurs due to the dearth of high-quality data regarding antisite defect concentrations in these compounds. The conventional understanding is that  $\text{Ni}^{2+}$  is about the same size as  $\text{Li}^+$ , so samples with more  $\text{Ni}^{2+}$  have more PAS defects. Our combination of exceptionally precise quantification of defect concentrations combined with a comprehensive set of samples spanning a wide range of NMC compositions provides an opportunity to gain new quantitative insights into the thermodynamics of defect formation.

In the prior literature, it is traditional to examine the variation of the concentration of Ni/Li PAS defects by plotting the dependence of the defect concentration (labeled as  $[\text{Ni}_{\text{Li}}]$ ) on sample composition or chemistry. Similar plots are shown for the present samples in Figure 4a–c. These three plots show the dependence on (a) the average Ni oxidation state, (b) the overall Ni content, and (c) the fractional concentration of  $\text{Ni}^{2+}$  relative to the total concentration of transition metals (Ni, Mn, and Co). From these three traditional plots, it is clear that (1) the correlation with the total PAS defect concentration is weak and (2) the behavior is often non-monotonic, with only the plot of the  $\text{Ni}^{2+}$  fraction appearing to be monotonic.

The reason for this behavior is apparent if one considers thermodynamic principles, which suggest that the energy cost for defect formation affects the probability of defect formation rather than the amount of defect formation. The data are therefore replotted in Figure 4d–f to show the variation in the percentage of Ni atoms, which reside in defect sites (labeled as %  $\text{Ni}_{\text{Li}}$ ). The systematic trends across NMC samples can be resolved from these plots. In all three plots, the smooth variation of %  $\text{Ni}_{\text{Li}}$  with composition suggests that the defect concentration in these samples is primarily determined by thermodynamic rather than kinetic considerations. If defect formation is a process that is simply driven by cation size, then the energy of Ni/Li PAS defect formation should be constant and the value of %  $\text{Ni}_{\text{Li}}$  should vary linearly with the average oxidation state of Ni (which is proportional to the percentage of Ni that exists as  $\text{Ni}^{2+}$  rather than  $\text{Ni}^{3+}$ ). However, the pertinent plot (Figure 4d) does not exhibit a simple linear dependence on the oxidation state (especially for low Ni oxidation states), suggesting that the energy of  $\text{Ni}_{\text{Li}}$  defect formation is not constant and that the conventional understanding of defect formation is incomplete.

An alternate explanation for the driving force of defect formation suggested by the present data is that the probability of defect formation depends on the size of the transition-metal site that Li occupies in  $\text{Li}_{\text{Ni}}$  defects and thus will depend indirectly rather than directly on the size of  $\text{Ni}^{2+}$  ions. In this picture, the amount of PAS defects should directly scale with the absolute amount of  $\text{Ni}^{2+}$  (Figure 4f) rather than the fraction of Ni ions present as  $\text{Ni}^{2+}$  (Figure 4d). It is indeed seen that the dependence of %  $\text{Ni}_{\text{Li}}$  on the total concentration of  $\text{Ni}^{2+}$  is linear (Figure 4f). This behavior occurs because the average size of transition-metal sites increases as the total amount of large  $\text{Ni}^{2+}$  ions in the layers increases, continually pushing apart the oxygens between which the transition metals

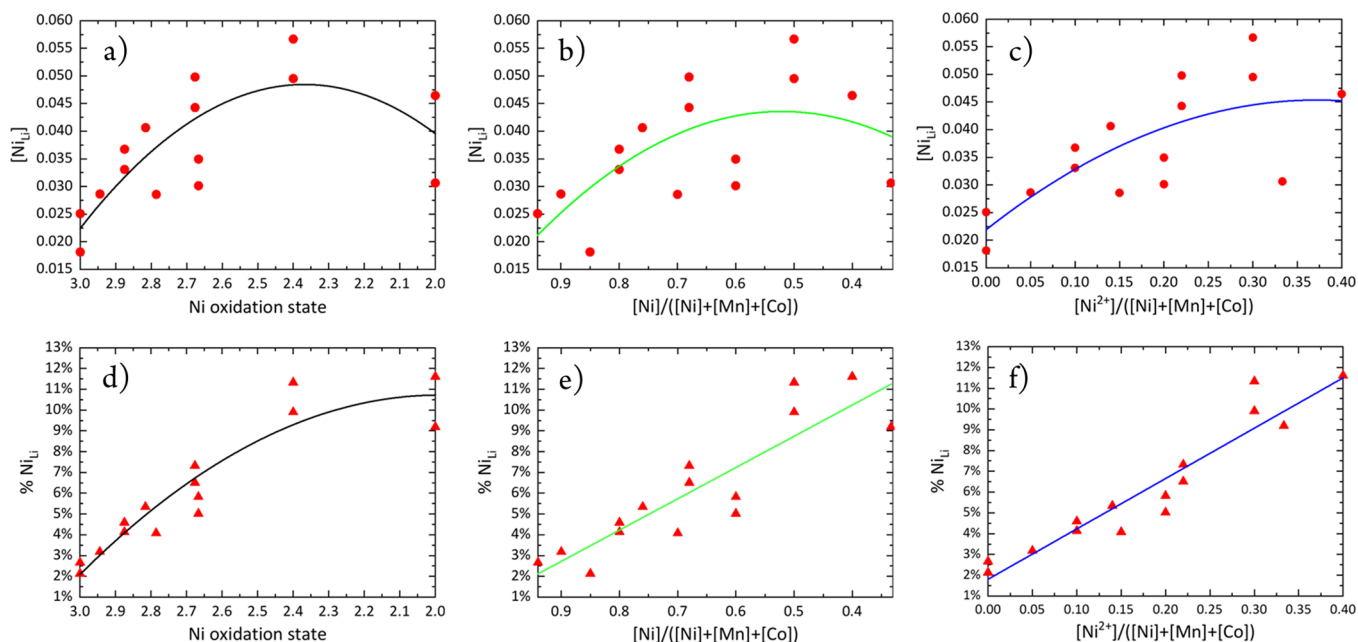


**Figure 4.** Variation of antisite defect concentration (top) or antisite defect fraction (bottom). Results are plotted either as a function of (a,d) the average Ni oxidation state, (b,e) the fraction of Ni (including both  $Ni^{2+}$  and  $Ni^{3+}$ ) relative to all transition metals, or (c,f) the fraction of  $Ni^{2+}$  relative to all transition metals for the 15 stoichiometric NMC samples studied in this work. Solid lines indicate best fits to a parabolic function (a–d) or a linear function (e,f).

reside in octahedral voids and expanding the transition-metal site size. This behavior is fully consistent with the general observation for solid-state compounds that unit cell volumes typically vary linearly with the degree of substitution (in the absence of discrete structural transitions). While it is also observed that  $\% Ni_{Li}$  varies nearly linearly with the total amount of Ni in the structure (Figure 4e), this behavior is less rigorously obeyed ( $R$ -squared value of linear fit of 0.78 vs 0.90 for the  $Ni^{2+}$  plot) and is mostly a consequence of the fact that  $Ni^{2+}$  is created through the incorporation of  $Mn^{4+}$ , a substitution that necessarily reduces the total amount of Ni in these NMC compounds (Figure S5). Our conclusion that the defect formation energy directly depends on the size of the crystallographic site rather than the  $Ni^{2+}$  ions is further supported by the observation that Ni/Li PAS defects are found in the two NMC compounds ( $LiNi_{0.85}Co_{0.15}O_2$  and  $LiNi_{0.94}Co_{0.06}O_2$ ), which lack  $Ni^{2+}$ , both of which have about 2% of their Ni ions residing on Li sites. Finally, our conclusion is closely supported by composition dependence of the defect formation energy, discussed in the next section.

Since the Ni/Li PAS defect concentration is primarily determined by thermodynamic considerations, it is possible to use the linear relationship observed between  $\% Ni_{Li}$  and  $[Ni^{2+}]$  to make predictions for the antisite defect concentration that will be observed for a sample of any NMC composition synthesized at a reaction temperature similar to those of the materials investigated in the present study (640–875 °C). The composition dependence of the proportion of and the total concentration of paired antisite  $Ni_{Li}$  and  $Li_{Ni}$  defects are plotted in Figure 5a,b based on the fit results from Figure 4f. It can be seen that the proportion of defects ( $\% Ni_{Li}$ ) has a very simple variation across the NMC compositional phase space relevant to battery applications (Figure 5a), with the defect proportion strictly depending on the transition-metal fraction of Mn, a quantity that directly determines the amount of  $Ni^{2+}$  in pristine NMC samples due to the charge balance

considerations. The total concentration of NMC defects (Figure 5b) shows a more complex behavior, as the defect concentration depends on both the total amount of Mn (which sets the proportion of Ni cations at defects sites) and the Ni:Co ratio (which influences the total amount of Ni). The antisite defect concentration for any NMC sample can be predicted within about 0.5% (absolute) using eq 1:

$$C_{\text{antisite}} = (0.2423 \times [Ni^{2+}] + 0.01808) \times [Ni] \quad (1)$$

This equation only applies to samples in the portion of the NMC phase diagram where all Mn is present as  $Mn^{4+}$  (below the  $LiCoO_2$ – $Li(Ni_{0.5}Mn_{0.5})O_2$  line) equilibrated at similar temperatures. In order to make predictions about PAS defect concentrations for samples equilibrated at different temperatures, information about the energetics of defect formation is required, as will be derived in the next section.

**Energy of Li/Ni PAS Defect Formation.** The Boltzmann relationship (eq 2) can be used to extract the energy associated with defect formation,  $\Delta E$ , from the proportion of Ni atoms in antisite defects determined using powder diffraction techniques:

$$\frac{\% \text{ of Ni on Li(3a) sites}}{\% \text{ of Ni on Ni(3b) sites}} = e^{-\Delta E/(k_B T)} \quad (2)$$

The quantity in the numerator is equal to  $\% Ni_{Li}$  discussed in the previous section, while the quantity in the denominator is  $(100\% - \% Ni_{Li})$ . Defect formation energies for the 15 stoichiometric NMC samples studied in this work are plotted in Figure 6a, with the extrapolated behavior based on the combined application of eqs 1 and 2 plotted as a blue curve, assuming a synthesis temperature of 1000 K for all samples. The energy for forming paired antisite defects of  $Ni_{Li}$  and  $Li_{Ni}$  monotonically decreases from 320 meV for the two samples with no  $Ni^{2+}$  to about 175 meV for the sample with the most  $Ni^{2+}$  (NMC442) studied in this work. If this behavior is

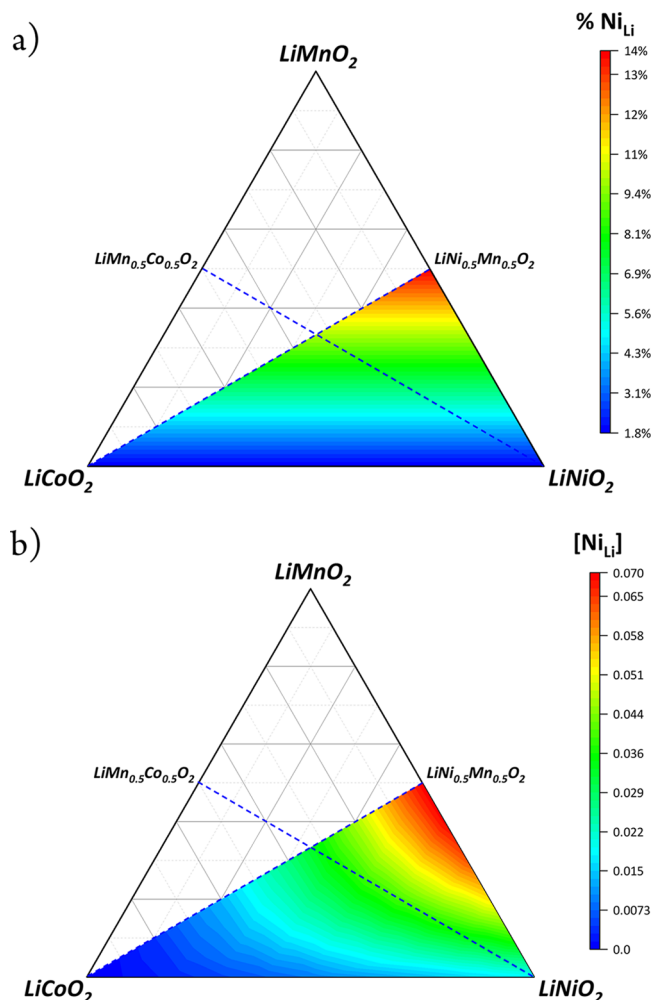


**Figure 5.** Dependence of antisite defect prevalence on composition. (a) Composition dependent variation of the fraction of Ni/Li paired antisite defects, % Ni<sub>Li</sub>, calculated from eq 1. (b) Composition-dependent variation of the concentration of Ni/Li paired antisite defects, [Ni<sub>Li</sub>], calculated from eq 2. Dashed lines indicate tie lines along which all Ni is present as Ni<sup>2+</sup> (LiCoO<sub>2</sub>–LiNi<sub>0.5</sub>Mn<sub>0.5</sub>O<sub>2</sub>) or along which the Mn and Co concentrations are equal (LiNiO<sub>2</sub>–LiMn<sub>0.5</sub>Co<sub>0.5</sub>O<sub>2</sub>). In Figure S6, positions of the NMC samples on this plot are marked.

extrapolated to the NMC composition of Li(Ni<sub>0.5</sub>Mn<sub>0.5</sub>)O<sub>2</sub>, the NMC composition with the highest achievable Ni<sup>2+</sup> fraction of 0.50, the energy of defect formation may drop to about 160 meV, consistent with the very high defect concentrations routinely observed for samples with this specific composition.<sup>31,32</sup>

While there have been prior theoretical investigations into the energetics of antisite defect formation using density functional theory (DFT), the DFT results have yet to demonstrate clear predictive value. This in part is due to the general challenges of using DFT to treat compounds with disorder, as different local configurations will necessarily lead to different defect energies, as well as necessitating the use of large and low-symmetry unit cells to capture these configurations. A recent DFT study<sup>33</sup> systematically studying the influence of NMC composition on antisite defect energy formation found that the calculated formation energy typically varied by hundreds of meV within different local transition-metal configurations for a single composition—a spread that

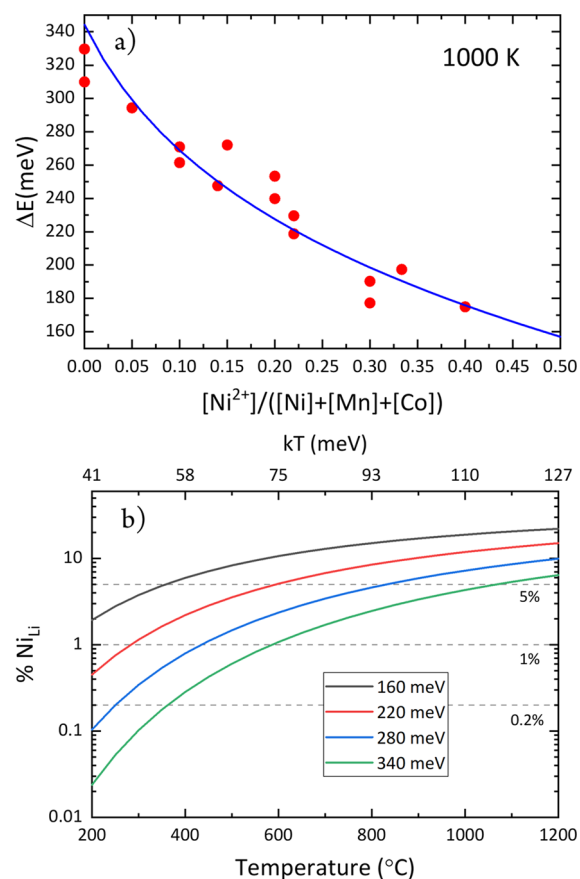


**Figure 6.** (a) Energy of paired antisite defect formation (calculated using the Boltzmann relationship under the assumption of equal multiplicity for the normal and defect states) as a function of the Ni<sup>2+</sup> transition-metal fraction in the NMC compound. The blue line is the transformation of the linear fit from Figure 4f. (b) Percentage of Ni atoms calculated that exist in Ni<sub>Li</sub> antisite defects as a function of equilibration temperature for four different activation energies characteristic of NMC samples ranging from 160 (estimated value for LiNi<sub>0.5</sub>Mn<sub>0.5</sub>O<sub>2</sub>) to 340 meV (LiNi<sub>1/3</sub>Mn<sub>1/3</sub>Co<sub>1/3</sub>O<sub>2</sub>). Note that the defect concentration, [Ni<sub>Li</sub>], is the product of the defect probability plotted here and the overall concentration of Ni<sup>2+</sup> in the NMC phase.

exceeds the ~150 meV span across all NMC compounds that were the subject of our present experimental investigation.

Additionally, relating the defect formation energy calculated by DFT to the actual defect concentration in synthesized samples requires knowledge of the multiplicity of configurations. In one recent comprehensive study of defects in Li(Ni<sub>1/3</sub>Mn<sub>1/3</sub>Co<sub>1/3</sub>)O<sub>2</sub>, a formation energy of 570 meV was calculated for Li/Ni PAS defects.<sup>34</sup> However, it was assumed that there was a multiplicity of six for the antisite defect pairs as opposed to only one for the structure in the absence of antisite defects, resulting in the effective energy for defect formation being nearly halved relative to what would be observed if both defect and defect-free systems had a single configuration. Even with this assumption, the calculated probability of defect formation (% Ni<sub>Li</sub> = 1.3% at 800 °C) was still about 10-fold lower than what was experimentally determined in this work. As such, the present experimental insights into defect formation energies within the structurally complex NMC compounds are more robust than theoretical alternatives.

At the synthesis temperature used to prepare these samples, the observed defect formation energies for the present samples typically range from about 2 to  $4k_{\text{B}}T$  (where  $k_{\text{B}}$  is the Boltzmann constant) for samples with high and low concentrations of  $\text{Ni}^{2+}$ , respectively, indicating that the equilibrium defect concentrations should be strongly sensitive to the equilibration temperature for all compositions. This temperature dependence is plotted in Figure 6b for samples with defect formation energies of 160 (black), 220 (blue), 280 (red), and 340 meV (green). In order to achieve  $\text{Ni}_{\text{Li}}$  defect probabilities of 1% or less, samples must be equilibrated at temperatures of about 300–500 °C or lower, temperatures at which the Ni cations may or may not be mobile. The Boltzmann relation can also be applied to predict the PAS defect concentration for any NMC composition equilibrated at any temperature by eq 3.

$$c_{\text{antisite}} = \frac{[\text{Ni}]}{1 + e^{\Delta E/(kT)}} \quad (3)$$

Complementary studies specifically investigating the kinetics associated with the formation and elimination of paired antisite defects are in progress and will be reported elsewhere.

## CONCLUSIONS

In conclusion, novel high-precision methods for determining antisite defect concentrations in NMC compounds using powder diffraction data have been used to provide clear thermodynamic insights into the energy of defect formation in the important class of NMC cathode materials. Based on these observations, it appears that defect formation is not purely driven by the size similarity of  $\text{Ni}^{2+}$  and  $\text{Li}^+$  as was previously believed but is more generally dependent on the average size of the transition-metal sites. The experimental results strongly differ from theoretical predictions, and it will be important to resolve the reason for this discrepancy. It is likely that a better understanding of the local structure of NMC compounds will be required to achieve this goal.

The present results suggest two main routes that should be followed for optimizing the paired antisite defect concentration to enhance the performance of NMC cathode materials. The first is through post-annealing samples to modify their defect concentration, utilizing the predictive guidance of the thermodynamic relationship developed in this work. While it is known that annealing NMC samples will affect their electrochemical performance, our work in developing advanced powder diffraction methods for defect quantification provides for the first time the opportunity to directly correlate electrochemical performance with accurately determined defect concentrations, work that is currently in progress. Second, it is expected that chemical substitution of larger or smaller cations at the transition-metal site can be used to modulate the antisite defect concentration to optimal levels. Although this strategy naturally follows from the results of the present work, this strategy would not have been judged as viable based on earlier hypotheses for the mechanism of antisite defect formation.

## ASSOCIATED CONTENT

### Supporting Information

The Supporting Information is available free of charge at <https://pubs.acs.org/doi/10.1021/acs.chemmater.9b03646>.

Refinement control (TXT)

TOPAS OUT files from Rietveld refinement of X-ray data (ZIP)

Raw synchrotron X-ray diffraction data of all NMCs (ZIP)

Refinement control (TXT)

TOPAS OUT files from Rietveld refinement of neutron data (ZIP)

Raw TOF neutron diffraction data for all NMCs (ZIP)

Structure figures, representative Rietveld fits to diffraction data, defect vectors in  $f^*$  diagrams, tabulated refinement results and synthesis conditions, additional plots of composition dependence of antisite defect concentration (PDF)

## AUTHOR INFORMATION

### Corresponding Author

**Peter G. Khalifah** – Department of Chemistry, Stony Brook University, Stony Brook, New York 11794, United States; Chemistry Division, Brookhaven National Laboratory, Upton, New York 11973, United States; [orcid.org/0000-0002-2216-0377](https://orcid.org/0000-0002-2216-0377); Email: [kpete@bnl.gov](mailto:kpete@bnl.gov)

### Authors

**Liang Yin** – Department of Chemistry, Stony Brook University, Stony Brook, New York 11794, United States; Chemistry Division, Brookhaven National Laboratory, Upton, New York 11973, United States

**Zhuo Li** – Department of Chemistry, Stony Brook University, Stony Brook, New York 11794, United States; Chemistry Division, Brookhaven National Laboratory, Upton, New York 11973, United States

**Gerard S. Mattei** – Department of Chemistry, Stony Brook University, Stony Brook, New York 11794, United States; Chemistry Division, Brookhaven National Laboratory, Upton, New York 11973, United States

**Jianming Zheng** – Energy and Environment Directorate, Pacific Northwest National Laboratory, Richland, Washington 99354, United States

**Wengao Zhao** – Energy and Environment Directorate, Pacific Northwest National Laboratory, Richland, Washington 99354, United States

**Fredrick Omenya** – Department of Chemistry, Binghamton University, Binghamton, New York 13902, United States

**Chengcheng Fang** – Department of NanoEngineering, University of California San Diego, La Jolla, California 92093, United States

**Wangda Li** – Materials Science and Engineering Program and Texas Materials Institute, The University of Texas at Austin, Austin, Texas 78712, United States; [orcid.org/0000-0001-8103-4285](https://orcid.org/0000-0001-8103-4285)

**Jianyu Li** – Materials Science and Engineering Program and Texas Materials Institute, The University of Texas at Austin, Austin, Texas 78712, United States

**Qiang Xie** – Materials Science and Engineering Program and Texas Materials Institute, The University of Texas at Austin, Austin, Texas 78712, United States

**Evan M. Erickson** – Materials Science and Engineering Program and Texas Materials Institute, The University of Texas at Austin, Austin, Texas 78712, United States

**Ji-Guang Zhang** – Energy and Environment Directorate, Pacific Northwest National Laboratory, Richland, Washington 99354, United States

**M. Stanley Whittingham** – Department of Chemistry, Binghamton University, Binghamton, New York 13902, United States; [orcid.org/0000-0002-5039-9334](https://orcid.org/0000-0002-5039-9334)

**Ying Shirley Meng** – Department of NanoEngineering, University of California San Diego, La Jolla, California 92093, United States; [orcid.org/0000-0001-8936-8845](https://orcid.org/0000-0001-8936-8845)

**Arumugam Manthiram** – Materials Science and Engineering Program and Texas Materials Institute, The University of Texas at Austin, Austin, Texas 78712, United States; [orcid.org/0000-0003-0237-9563](https://orcid.org/0000-0003-0237-9563)

Complete contact information is available at:  
<https://pubs.acs.org/10.1021/acs.chemmater.9b03646>

## Notes

The authors declare no competing financial interest.

## ACKNOWLEDGMENTS

This work was supported by the Assistant Secretary for Energy Efficiency and Renewable Energy, Office of Vehicle Technologies of the U.S. Department of Energy (DOE) through the Advanced Battery Materials Research (BMR) program and the Battery500 Consortium under Contract No. DE-SC0012704. Use of the Advanced Photon Source at the Argonne National Laboratory was supported by the U.S. Department of Energy, Office of Science, Office of Basic Energy Sciences, under Contract No. DE-AC02-06CH11357. A portion of this research used resources at the Spallation Neutron Source, a DOE Office of Science User Facility operated by the Oak Ridge National Laboratory. Y.S.M. and C.F. thank Dr. Bao Qiu from Ningbo Institute of Materials Technology and Engineering NIMTE for providing a BASF 333 sample. Support and training from NOMAD beamline team members including Katharine Page, Michelle Everett, and Joerg C. Neufeind are gratefully acknowledged, as is the work of Jonathan Denney in writing automated codes to verify  $f^*$  diagram calculations.

## REFERENCES

- Rougier, A.; Gravereau, P.; Delmas, C. Optimization of the Composition of the  $\text{Li}_{1-x}\text{Ni}_{1+x}\text{O}_2$  Electrode Materials: Structural, Magnetic, and Electrochemical Studies. *J. Electrochem. Soc.* **1996**, *143*, 1168–1175.
- Dahn, J. R.; von Sacken, U.; Michal, C. A. Structure and electrochemistry of  $\text{Li}_{1\pm x}\text{NiO}_2$  and a new  $\text{Li}_2\text{NiO}_2$  phase with the  $\text{Ni}(\text{OH})_2$  structure. *Solid State Ionics* **1990**, *44*, 87–97.
- Delmas, C.; Pères, J. P.; Rougier, A.; Demourgues, A.; Weill, F.; Chadwick, A.; Broussely, M.; Pertont, F.; Biensan, P.; Willmann, P. On the behavior of the  $\text{Li}_x\text{NiO}_2$  system: an electrochemical and structural overview. *J. Power Sources* **1997**, *68*, 120–125.
- Neufeind, J.; Feygenson, M.; Carruth, J.; Hoffmann, R.; Chipley, K. K. The Nanoscale Ordered MAterials Diffractometer NOMAD at the Spallation Neutron Source SNS. *Nucl. Instrum. Methods Phys. Res., Sect. B* **2012**, *287*, 68–75.
- Shankland, K.; David, W.; McCusker, L.; Baerlocher, C. *Structure determination from powder diffraction data*; Oxford University Press, Incorporated: New York, 2006.
- Young, R. A. *The Rietveld Method*; Oxford University Press: New York, 1995.
- Dinnebier, R. E.; Billinge, S. J. *Powder diffraction: theory and practice*; Royal Society of Chemistry: Cambridge, 2008, DOI: 10.1039/9781847558237.
- Toby, B. H. R factors in Rietveld analysis: How good is good enough? *Powder Diff.* **2006**, *21*, 67–70.
- Rougier, A.; Saadoun, I.; Gravereau, P.; Willmann, P.; Delmas, C. Effect of cobalt substitution on cationic distribution in  $\text{LiNi}_{1-y}\text{Co}_y\text{O}_2$  electrode materials. *Solid State Ionics* **1996**, *90*, 83–90.

(10) Cho, J.; Kim, G.; Lim, H. S. Effect of Preparation Methods of  $\text{LiNi}_{1-x}\text{Co}_x\text{O}_2$  Cathode Materials on Their Chemical Structure and Electrode Performance. *J. Electrochem. Soc.* **1999**, *146*, 3571–3576.

(11) Lu, Z.; Beaulieu, L. Y.; Donaberger, R. A.; Thomas, C. L.; Dahn, J. R. Synthesis, Structure, and Electrochemical Behavior of  $\text{Li}[\text{Ni}_x\text{Li}_{1/3-2x/3}\text{Mn}_{2/3-x/3}]\text{O}_2$ . *J. Electrochem. Soc.* **2002**, *149*, A778–A791.

(12) MacNeil, D. D.; Lu, Z.; Dahn, J. R. Structure and Electrochemistry of  $\text{Li}[\text{Ni}_x\text{Co}_{1-2x}\text{Mn}_x]\text{O}_2$  ( $0 \leq x \leq 1/2$ ). *J. Electrochem. Soc.* **2002**, *149*, A1332–A1336.

(13) Lu, Z.; Chen, Z.; Dahn, J. R. Lack of Cation Clustering in  $\text{Li}[\text{Ni}_x\text{Li}_{1/3-2x/3}\text{Mn}_{2/3-x/3}]\text{O}_2$  ( $0 < x \leq 1/2$ ) and  $\text{Li}[\text{Cr}_x\text{Li}_{(1-x)/3}\text{Mn}_{(2-x)/3}]\text{O}_2$  ( $0 < x < 1$ ). *Chem. Mater.* **2003**, *15*, 3214–3220.

(14) Ngala, J. K.; Chernova, N. A.; Ma, M.; Mamak, M.; Zavalij, P. Y.; Whittingham, M. S. The synthesis, characterization and electrochemical behavior of the layered  $\text{LiNi}_{0.4}\text{Mn}_{0.4}\text{Co}_{0.2}\text{O}_2$  compound. *J. Mater. Chem.* **2004**, *14*, 214–220.

(15) Shizuka, K.; Kobayashi, T.; Okahara, K.; Okamoto, K.; Kanzaki, S.; Kanno, R. Characterization of  $\text{Li}_{1+y}\text{Ni}_x\text{Co}_{1-2x}\text{Mn}_x\text{O}_2$  positive active materials for lithium ion batteries. *J. Power Sources* **2005**, *146*, 589–593.

(16) Yin, S.-C.; Rho, Y.-H.; Swainson, I.; Nazar, L. F. X-ray/Neutron Diffraction and Electrochemical Studies of Lithium De/Re-Intercalation in  $\text{Li}_{1-x}\text{Co}_{1/3}\text{Ni}_{1/3}\text{Mn}_{1/3}\text{O}_2$  ( $x = 0 \rightarrow 1$ ). *Chem. Mater.* **2006**, *18*, 1901–1910.

(17) Kosova, N. V.; Devyatkina, E. T.; Kaichev, V. V.  $\text{LiNi}_{1-x-y}\text{Co}_x\text{Mn}_y\text{O}_2$  ( $x = y = 0.1, 0.2, 0.33$ ) cathode materials prepared using mechanical activation: Structure, state of ions, and electrochemical performance. *Inorg. Mater.* **2007**, *43*, 185–193.

(18) Reale, P.; Privitera, D.; Panero, S.; Scrosati, B. An investigation on the effect of  $\text{Li}^+/\text{Ni}^{2+}$  cation mixing on electrochemical performances and analysis of the electron conductivity properties of  $\text{LiCo}_{0.33}\text{Mn}_{0.33}\text{Ni}_{0.33}\text{O}_2$ . *Solid State Ionics* **2007**, *178*, 1390–1397.

(19) Lee, K.-S.; Myung, S.-T.; Prakash, J.; Yashiro, H.; Sun, Y.-K. Optimization of microwave synthesis of  $\text{Li}[\text{Ni}_{0.4}\text{Co}_{0.2}\text{Mn}_{0.4}]\text{O}_2$  as a positive electrode material for lithium batteries. *Electrochim. Acta* **2008**, *53*, 3065–3074.

(20) Zhang, X.; Jiang, W. J.; Mauger, A.; Qilu, Gendron, F.; Julien, C. M. Minimization of the cation mixing in  $\text{Li}_{1+x}(\text{NMC})_{1-x}\text{O}_2$  as cathode material. *J. Power Sources* **2010**, *195*, 1292–1301.

(21) Gu, Y.-J.; Chen, Y.-B.; Liu, H.-Q.; Wang, Y.-M.; Wang, C.-L.; Wu, H.-K. Structural characterization of layered  $\text{Li-Ni}_{0.85-x}\text{Mn}_x\text{Co}_{0.15}\text{O}_2$  with  $x = 0, 0.1, 0.2$  and  $0.4$  oxide electrodes for Li batteries. *J. Alloys Compd.* **2011**, *509*, 7915–7921.

(22) Kumar, P. S.; Sakunthala, A.; Reddy, M. V.; Shanmugam, S.; Prabhu, M. Correlation between the structural, electrical and electrochemical performance of layered  $\text{Li}(\text{Ni}_{0.33}\text{Co}_{0.33}\text{Mn}_{0.33})\text{O}_2$  for lithium ion battery. *J. Solid State Electrochem.* **2016**, *20*, 1865–1876.

(23) Wu, F.; Tian, J.; Su, Y.; Wang, J.; Zhang, C.; Bao, L.; He, T.; Li, J.; Chen, S. Effect of  $\text{Ni}^{2+}$  content on lithium/nickel disorder for Ni-rich cathode materials. *ACS Appl. Mater. Interfaces* **2015**, *7*, 7702–7708.

(24) Zheng, J.; Kan, W. H.; Manthiram, A. Role of Mn Content on the Electrochemical Properties of Nickel-Rich Layered  $\text{Li-Ni}_{0.8-x}\text{Co}_{0.1}\text{Mn}_{0.1+x}\text{O}_2$  ( $0.0 \leq x \leq 0.08$ ) Cathodes for Lithium-Ion Batteries. *ACS Appl. Mater. Interfaces* **2015**, *7*, 6926–6934.

(25) Yoon, C. S.; Choi, M.-J.; Jun, D.-W.; Zhang, Q.; Kaghazchi, P.; Kim, K.-H.; Sun, Y.-K. Cation Ordering of Zr-Doped  $\text{LiNiO}_2$  Cathode for Lithium-Ion Batteries. *Chem. Mater.* **2018**, *30*, 1808–1814.

(26) Kobayashi, H.; Sakaebe, H.; Kageyama, H.; Tatsumi, K.; Arachi, Y.; Kamiyama, T. Changes in the structure and physical properties of the solid solution  $\text{LiNi}_{1-x}\text{Mn}_x\text{O}_2$  with variation in its composition. *J. Mater. Chem.* **2003**, *13*, 590–595.

(27) Zhao, J.; Zhang, W.; Huq, A.; Mixture, S. T.; Zhang, B.; Guo, S.; Wu, L.; Zhu, Y.; Chen, Z.; Amine, K.; Pan, F.; Bai, J.; Wang, F. In Situ Probing and Synthetic Control of Cationic Ordering in Ni-Rich Layered Oxide Cathodes. *Adv. Energy Mater.* **2017**, *7*, 1601266.

(28) Wang, D.; Kou, R.; Ren, Y.; Sun, C.-J.; Zhao, H.; Zhang, M.-J.; Li, Y.; Huq, A.; Ko, J. Y. P.; Pan, F.; Sun, Y.-K.; Yang, Y.; Amine, K.; Bai, J.; Chen, Z.; Wang, F. Synthetic Control of Kinetic Reaction Pathway and Cationic Ordering in High-Ni Layered Oxide Cathodes. *Adv. Mater.* **2017**, *29*, 1606715.

(29) Cai, L.; Liu, Z.; An, K.; Liang, C. Probing Li-Ni Cation Disorder in  $\text{Li}_{1-x}\text{Ni}_{1+x-y}\text{Al}_y\text{O}_2$  Cathode Materials by Neutron Diffraction. *J. Electrochem. Soc.* **2012**, *159*, A924–A928.

(30) Yin, L.; Mattei, G. S.; Li, Z.; Zheng, J.; Zhao, W.; Omenya, F.; Fang, C.; Li, W.; Li, J.; Xie, Q.; Zhang, J. G.; Whittingham, M. S.; Meng, Y. S.; Manthiram, A.; Khalifah, P. G. Extending the limits of powder diffraction analysis: Diffraction parameter space, occupancy defects, and atomic form factors. *Rev. Sci. Instrum.* **2018**, *89*, No. 093002.

(31) Bréger, J.; Meng, Y. S.; Hinuma, Y.; Kumar, S.; Kang, K.; Shao-Horn, Y.; Ceder, G.; Grey, C. P. Effect of high voltage on the structure and electrochemistry of  $\text{LiNi}_{0.5}\text{Mn}_{0.5}\text{O}_2$ : A joint experimental and theoretical study. *Chem. Mater.* **2006**, *18*, 4768–4781.

(32) Kang, K.; Meng, Y. S.; Bréger, J.; Grey, C. P.; Ceder, G. Electrodes with High Power and High Capacity for Rechargeable Lithium Batteries. *Science* **2006**, *311*, 977–980.

(33) Zheng, J.; Teng, G.; Xin, C.; Zhuo, Z.; Liu, J.; Li, Q.; Hu, Z.; Xu, M.; Yan, S.; Yang, W.; Pan, F. Role of Superexchange Interaction on Tuning of Ni/Li Disorder in Layered  $\text{Li}(\text{Ni}_x\text{Mn}_y\text{Co}_z)\text{O}_2$ . *J. Phys. Chem. Lett.* **2017**, *8*, 5537–5542.

(34) Hoang, K.; Johannes, M. Defect Physics and Chemistry in Layered Mixed Transition Metal Oxide Cathode Materials: (Ni,Co,Mn) vs (Ni,Co,Al). *Chem. Mater.* **2016**, *28*, 1325–1334.